# Iterative minimization in reduced density matrix functional theory for periodic systems

Kai Luo,[1,*] Jingang Han,[2,3] Peize Lin,[4] Daye Zheng,[5] Mohan Chen,[6] and Xinguo Ren[2,†]

[1] *Department of Applied Physics, Nanjing University of Science and Technology, Nanjing 210094, China*
[2] *Institute of Physics, Chinese Academy of Sciences, Beijing 100190, China*
[3] *School of Physical Sciences, University of Chinese Academy of Sciences, Beijing 100049, China*
[4] *University of Science and Technology of China, Hefei 230026, China*
[5] *AI for Science Institute, Beijing 100080, P. R. China*
[6] *HEDPS, CAPT, School of Mechanics and Engineering Science and School of Physics, Peking University, Beijing, 100871, P. R. China*

(Dated: prepared on Jul 30, 2026)

Reduced density matrix functional theory (RDMFT) offers a route beyond Kohn-Sham density functional theory for strongly correlated systems, yet practical calculations for periodic solids are still out of reach. We formulate RDMFT for extended systems in a basis-independent way and present a planewave implementation using iterative minimization for periodic solids, evaluating nonlocal exchange-correlation functionals through the existing adaptive compressed exchange machinery. Natural occupations are optimized under N-representability constraints with a spectral projected gradient (SPG) method or an first-order explicit-by-implicit (EBI) map, while natural orbitals are updated by Riemannian optimization on the complex Stiefel manifolds. Benchmarks on typical systems of $H_2$, silicon, and sodium with the Hartree-Fock functional show that SPG reproduces converged hybrid references, whereas EBI can stall when occupations approach 0 or 1. With the power and Müller functionals, SPG yields lower energies and more stable convergence than EBI. Applications to fractionally charged LiH, dissociating $H_2$ and $N_2$ molecules, and equation of state of silicon show that the algorithm presented in this implementation is reliable and robust.

arXiv:2607.27679v1 [cond-mat.str-el] 30 Jul 2026

## I. INTRODUCTION

For decades, the Kohn-Sham density functional theory (DFT) [1, 2] has been the most widely used method in chemistry and materials science for finite and extended systems. However, it faces challenges in handling systems where the delocalization errors and strong correlations play a central role. Reduced density matrix functional theory (RDMFT) [3, 4] provides a promising alternative *ab initio* approach to overcome the inherent limitations of DFT by going beyond the idempotency constraint on the one-body reduced density matrix (1-RDM). Gilbert's extension of the Hohenberg-Kohn theorem to nonlocal external potentials provides the formal basis for treating the ground-state energy as a functional of the one-body reduced density matrix (1-RDM) [3]. Because the 1-RDM retains orbital information and admits non-idempotent spectra, it is a natural language for bond dissociation, near degeneracy, and correlated insulating behavior [5].

The practical performance of RDMFT depends on two key factors: the accuracy of the approximation chosen for the exchange-correlation (XC) functional and the efficiency and robustness of the solver for finding the density matrix solution. Early and still influential XC functionals include Müller's functional [4] (or the BB functional [6]), the Goedecker-Umrigar self-interaction-corrected variant [7]. For molecules, a family of BB-corrected functionals to fix BB's overcorrelation problem have been developed based on notion of strong and weak occupation [8]. Interestingly, Csányi and collaborators constructed CHF and CGA functionals from a tensor-product ansatz[9, 10]. Piris and collaborators developed another family of natural-orbital functionals, known as PNOF$i$ ($i = 1$–$7$), by approximating the cumulant matrix subject to known constraints on the two-body reduced density matrix $\Gamma$. Pernal established a correspondence between the PNOF5 functional and the antisymmetrized product of strongly orthogonal geminals [11]. Motivated by range separation, related hybrids combine a density-functional approximation at short range with the long-range Müller functional [12, 13]. For periodic solids, partly due to the lack of packages, there are fewer functionals and their performance is not well studied. So far, the power functional introduced by Sharma *et al.* extended RDMFT beyond molecules and atoms, showing that fractional powers of the 1-RDM can reproduce band gaps in ordinary semiconductors and open correlated gaps in Mott insulators[14]. The improved CGA functional was meant to treat solids by matching the uniform electron gas (UEG) correlation, but its performance is still unknown.

* kluo@njust.edu.cn
† renxg@iphy.ac.cn

Further work aligning with UEG correlation by Baldsiefen *et al.* at zero temperature led to a few functionals, but no systematic study has been done yet [15].

The other key factor is the numerical bottleneck for solving the density matrix equation. Recently, Vladaj *et al.* proposed a variational minimization scheme for functionals of the 1-RDM in the ensemble N-representable domain to solve the density matrix equation [16], which seems quite efficient on the Hubbard model and hydrogen molecule. A more general approach is necessary to include versatile functionals that is not restricted to 1-RDM only functionals. Following the conventional spectral decomposition, the density matrix is represented by the natural orbitals and their associated natural occupation numbers. Natural occupations must satisfy N-representability, orbitals must remain orthonormal in either Euclidean or overlap-weighted metrics, and the total energy is generally nonconvex in the combined variables. These issues become more pronounced in periodic calculations, where spin channels, $k$-point weights, and nonlocal exchange-like operators must be handled together. Efficient implementations therefore require more than a formal XC functional: they need stable constraint handling, geometry-aware orbital optimization, and high performance exact-exchange (EXX) evaluation in a parallel layout that can serve both molecules and solids. Most implementations for RDMFT calculations are based on existing quantum chemistry packages, which are mostly oriented for molecules and clusters. It is worth noting that an open-source solution provided by DoNOF [17, 18] sets a good example for accessible algorithms for RDMFT development. So far, as far as we know, only the LAPW package ELK [19] can perform such calculations for solids. There these natural orbitals are expanded in a set of converged KS orbitals and EXX matrix elements are stored locally on the hard-disk. Therefore, the implementation lacks the flexibility and efficiency for general applications.

Here we provide a basis-independent formulation of RDMFT for periodic solids and implement it as a self-consistent-field module in a massively parallel planewave code, Quantum ESPRESSO (QE)[20]. While natural orbitals are updated by Riemannian optimization on complex Stiefel manifolds following our previous work [21], natural occupations are optimized under N-representability constraints with the spectral projected gradient (SPG) method. The explicit-by-implicit (EBI) map of first-order is included for comparison. We evaluate nonlocal XC functionals through the adaptive compressed exchange (ACE) [22] framework that is already used in hybrid calculations. Representative benchmarks on molecules and bulk ($H_2$, silicon, and sodium) show that this workflow is numerically stable and suitable for general solid-state applications.

The remainder of the paper is organized as follows. Section II develops a basis-independent RDMFT formulation for periodic systems, including the $k$-resolved spectral representation of the 1-RDM, XC functionals and their evaluation, the constrained energy minimization problem, and the alternating updates for natural occupations via SPG or EBI and for natural orbitals on complex Stiefel manifolds. Section III describes the planewave implementation in QE, where XC functionals are evaluated through ACE and analytical gradients are verified against finite differences. Section IV presents Hartree-Fock (HF) and power functional benchmarks of SPG against EBI, tests of initial-occupation robustness, and applications to fractionally charged LiH, molecular dissociation, and the silicon equation of state. Section V concludes with a summary and outlook.

## II. THEORY

### A. Reduced density matrix functional theory

We consider the systems of interacting electrons governed by the Hamiltonian

$$\hat{H} = \hat{T} + \hat{V} + \hat{W}, \tag{1}$$

with the kinetic energy $\hat{T}$, the external one-body potential $\hat{V}$, and the two-body electron-electron interaction $\hat{W}$, respectively. The ground-state energy is achieved by variationally minimizing the Hamiltonian with respect to the wave function $\Psi$. In RDMFT, the ground-state energy can be obtained by minimizing the energy $E[\gamma]$ as a functional of 1-RDM, $\gamma(x, x')$, for fixed number of electrons $N$. Here $x$ is a composite of the spatial and spin coordinates, $x = (\mathbf{r}, \sigma)$. Following the conventional decomposition of the energy, we may write

$$E[\gamma] = E_k[\gamma] + E_{\mathrm{H}}[\gamma] + E_{\mathrm{xc}}[\gamma] + V[\gamma]. \tag{2}$$

These functionals of kinetic energy, Hartree energy, and external potential energy are

$$E_k[\gamma] = \int dx' \lim_{\mathbf{r}\to\mathbf{r}'} \left(-\frac{\nabla^2}{2}\right) \gamma(x,x'), \tag{3}$$

$$E_{\mathrm{H}}[\gamma] = \frac{1}{2}\int dx dx' w(x,x')\,\gamma(x,x)\gamma(x',x'), \tag{4}$$

$$V[\gamma] = \int dx \int dx' v(x,x')\,\gamma(x',x), \tag{5}$$

where $w(\mathbf{r},\mathbf{r}')$ is the electron-electron interaction potential (e.g. $1/|\mathbf{r}-\mathbf{r}'|$ for Coulomb interaction) and the external potential $v(x,x')$ is kept nonlocal in general. At finite temperature $T$, the free energy $F[\gamma]$ is given by adding the entropic energy, $F[\gamma] = E[\gamma] - TS[\gamma]$. The entropy can be computed from the natural occupation numbers $n_i$,

$$S[\gamma] = -k_B \sum_i \left[n_i \ln n_i + (1-n_i)\ln(1-n_i)\right], \tag{6}$$

where $k_B$ is the Boltzmann constant. This formula also defines the XC energy, which should include the difference of the entropy term between the interacting and non-interacting systems. The exact form of XC energy $E_{\mathrm{xc}}[\gamma]$ is unknown and has to be approximated; Sec. II B summarizes the XC functionals used in this work.

Diagonalization of the Hermitian $\gamma(x,x')$, yields the natural occupation numbers $n_i$ and natural orbitals $\psi_i(x)$, which gives the spectral representation of the 1-RDM [23],

$$\gamma(x,x') = \sum_i n_i \psi_i(x)\psi_i^*(x'). \tag{7}$$

The N-representability condition for 1-RDM was solved by Coleman [24, 25]. The theorem states that the 1-RDM is N-representable if and only if the natural occupation numbers are in the interval [0,1] and the sum of the natural occupation numbers is equal to the number of electrons. Mathematically, it can be summarized as the following constraints:

$$\sum_i^{N_{\mathrm{b}}} n_i = N, \quad 0 \le n_i \le 1, \tag{8}$$

where $N_{\mathrm{b}}$ is the number of occupied natural orbitals and $N$ is the number of electrons. For the cuspy Coulomb interaction at zero temperature, an infinite number of natural orbitals in principle is required to fully represent the non-idempotent 1-RDM, namely $N_{\mathrm{b}} \to \infty$. In practice, $N_{\mathrm{b}}$ is typically limited by the number of basis functions. Often, $N_{\mathrm{b}}$ could be further limited to a minimum number, especially for these idempotent density matrices in HF theory or DFT.

Under the periodic boundary conditions, $\gamma$ can be written as a sum of $\mathbf{k}$-resolved 1-RDMs,

$$\gamma(\mathrm{x},\mathrm{x}') = \sum_{\mathbf{k}} w_{\mathbf{k}} \gamma_{\mathbf{k}}(\mathrm{x},\mathrm{x}'). \tag{9}$$

In the collinear spin-polarized case, the $\mathbf{k}$-resolved 1-RDM $\gamma_{\mathbf{k}}(\mathrm{x},\mathrm{x}')$ is diagonal in spin, and it can be written in the spectral form as

$$\gamma_{\mathbf{k}}(\mathrm{x},\mathrm{x}') = \delta_{\sigma\sigma'} \sum_{i=1}^{N_{\mathrm{b}}} n_{i\mathbf{k}\sigma}\, \psi_{i\mathbf{k}}(\mathrm{x})\, \psi_{i\mathbf{k}}^*(\mathrm{x}'). \tag{10}$$

These natural orbitals $\psi_{i\mathbf{k}}$ follow the Bloch theorem by the translational symmetry of the $\mathbf{k}$-resolved 1-RDM. For periodic systems, $w_{\mathbf{k}}$ are Brillouin-zone weights normalized so that $\sum_{\mathbf{k}} w_{\mathbf{k}} = 1$ in a spin-polarized calculation (or 2 in the usual spin-restricted closed-shell convention where the trace over spin is absorbed into weights). For collinear spin-polarized calculations, the spin densities $\rho_\sigma(\mathbf{r}) = \gamma(\mathbf{r}\sigma,\mathbf{r}\sigma)$ ($\sigma = \uparrow,\downarrow$) sum to $\rho(\mathbf{r}) = \rho_\uparrow(\mathbf{r}) + \rho_\downarrow(\mathbf{r})$, and collinear magnetization profiles use $m_z(\mathbf{r}) = \rho_\uparrow(\mathbf{r}) - \rho_\downarrow(\mathbf{r})$. In addition to the electron number constraint $\sum_{i\mathbf{k}\sigma} w_{\mathbf{k}} n_{i\mathbf{k}\sigma} = N_e$, a fixed magnetization $M_z$ can be enforced with an additional Lagrange multiplier on $\sum_{i\mathbf{k}} w_{\mathbf{k}}(n_{i\mathbf{k}\uparrow} - n_{i\mathbf{k}\downarrow}) - M_z$. Isolated systems such as atoms and molecules correspond to the $\Gamma$-only limit, and $w_\Gamma = 1$, so Eq. (9) covers both finite and extended systems without changing notation.

TABLE I. XC couplings used in the present formulation. For separable forms, $f(n_i, n_j) = g(n_i)\, g(n_j)$. For the power functional, $\alpha \in (\frac{1}{2}, 1)$; values $\alpha \approx 0.656$ (periodic semiconductors) and $\alpha \approx 0.525$ (molecular dissociation) appear in the literature [14]. Mixed functionals whose terms are each of the form $g(n_i)\, g(n_j)$ are separable and evaluated as sums of ACE channels.

| Functional | $f(n_i, n_j)$ | Separability / channels |
|---|---|---|
| HF | $n_i n_j$ | Separable; $g(n) = n$ |
| Müller [4] | $\sqrt{n_i n_j}$ | Separable; $g(n) = n^{1/2}$ |
| Power [14] | $n_i^\alpha n_j^\alpha$ | Separable; $g(n) = n^\alpha$ |
| Goedecker-Umrigar [7] | $\sqrt{n_i n_j}$ for $i \neq j$, $n_i^2$ for $i = j$ | Separable |
| CHF [9] | $\frac{1}{2} n_i n_j + \frac{1}{2}\sqrt{n_i(1-n_i)}\sqrt{n_j(1-n_j)}$ | Separable; 2 channels |
| CGA [10] | $\frac{1}{4} n_i n_j + \frac{1}{4}\sqrt{n_i(2-n_i)}\sqrt{n_j(2-n_j)}$ | Separable; 2 channels |
| BOW [15] | $(n_i n_j)^\alpha - \alpha n_i n_j + \alpha - \alpha(1 - n_i n_j)^{1/\alpha}$, $\alpha = 0.61$ | Non-separable |

These Bloch natural orbitals $\psi_{i\mathbf{k}}$ are mutually orthogonal within each $\mathbf{k}$ block [Eq. (12)] and are normally expanded in a Bloch basis $\{\chi_{\mu\mathbf{k}}\}$,

$$\psi_{i\mathbf{k}}(\mathbf{r}) = \sum_{\mu=1}^{N_{\text{basis}}} C_{\mu i\mathbf{k}}\, \chi_{\mu\mathbf{k}}(\mathbf{r})\,. \tag{11}$$

The dimension of the basis set is $N_{\text{basis}}$, with $N_{\text{basis}} \geq N_{\text{b}}$. The expansion coefficients $C_{\mu i\mathbf{k}}$ can be regarded as a matrix whose $i$th column contains the expansion coefficients of the $i$th natural orbital indexed by $\mathbf{k}$. Its dimension is $N_{\text{basis}} \times N_{\text{b}}$ and it is shortly denoted as $\mathsf{C}_\mathbf{k}$.

In general, the overlap matrix for orthogonal basis (e.g. planewave basis) is simply the identity matrix $\mathsf{I}_{N_{\text{basis}}}$. Orthonormality of natural orbitals implies

$$(\mathsf{C}_\mathbf{k})^\dagger \mathsf{S}_\mathbf{k} \mathsf{C}_\mathbf{k} = \mathsf{I}_{N_{\text{b}}}, \tag{12}$$

with overlap matrix $(\mathsf{S}_\mathbf{k})_{\mu\nu} \equiv \langle \chi_{\mu\mathbf{k}} | \chi_{\nu\mathbf{k}} \rangle$. Collecting the occupation numbers $n_{i\mathbf{k}}$ into a vector $\mathsf{n}_\mathbf{k}$, the 1-RDM in the basis set $\{\chi_{\mu\mathbf{k}}\}$ can be compactly written in the matrix form as

$$\gamma_\mathbf{k} = \mathsf{C}_\mathbf{k}\ \mathrm{diag}(\mathsf{n}_\mathbf{k})\, \mathsf{C}_\mathbf{k}^\dagger, \tag{13}$$

when $\mathrm{diag}(\mathsf{v})$ is a diagonal matrix with elements $v_i \delta_{ij}$. The electron density is given by the diagonal of the 1-RDM,

$$\rho(x) = \gamma(x, x')\big|_{x'=x} = \sum_\mathbf{k} w_\mathbf{k} \sum_i n_{i\mathbf{k}\sigma} \rho_{i\mathbf{k}}(x)\,, \tag{14}$$

where each orbital density $\rho_{i\mathbf{k}}(x)$ can be obtained from these coefficient matrices $\mathsf{C}_\mathbf{k}$ via

$$\rho_{i\mathbf{k}}(x) = |\psi_{i\mathbf{k}}(x)|^2 = \sum_{\mu,\nu}^{N_{\text{basis}}} C_{\mu i\mathbf{k}} C^*_{\nu i\mathbf{k}} \chi_{\mu\mathbf{k}}(x) \chi^*_{\nu\mathbf{k}}(x). \tag{15}$$

### B. Exchange-correlation functionals

The XC energy $E_{\text{xc}}[\gamma]$ is a functional of the full 1-RDM rather than of the density alone. In the natural-orbital representation,

$$E_{\text{xc}} = -\frac{1}{2} \sum_{\mathbf{k},\mathbf{k}'} w_\mathbf{k}\, w_{\mathbf{k}'} \sum_{ij} f(n_{i\mathbf{k}}, n_{j\mathbf{k}'}) \iint \frac{\psi^*_{i\mathbf{k}}(\mathbf{r})\, \psi^*_{j\mathbf{k}'}(\mathbf{r}')\, \psi_{i\mathbf{k}}(\mathbf{r}')\, \psi_{j\mathbf{k}'}(\mathbf{r})}{|\mathbf{r} - \mathbf{r}'|}\, \mathrm{d}\mathbf{r}\, \mathrm{d}\mathbf{r}', \tag{16}$$

where $f(n_i, n_j)$ is a pair kernel acting on natural-occupation pairs. Table I lists commonly used XC functionals and their pair kernels $f(n_i, n_j)$. When the pair kernel can be written as a sum of terms, each of which factorises as

$$f(n_{i\mathbf{k}}, n_{j\mathbf{k}'}) = g(n_{i\mathbf{k}})\, g(n_{j\mathbf{k}'}), \tag{17}$$

it is said to be *separable*, with single-occupation coupling function $g(n)$. In this work we restrict to separable functionals; non-separable kernels such as the BOW functional [15] require the full pair and are substantially more costly to evaluate.

In a planewave basis, Eq. (16) with the separable form of Eq. (17) becomes

$$E_{\rm xc} = -\frac{1}{2}\sum_{\mathbf{k},\mathbf{k}'} w_{\mathbf{k}}\, w_{\mathbf{k}'} \sum_{ij} g(n_{i\mathbf{k}})\, g(n_{j\mathbf{k}'}) \sum_{\mathbf{G}} \frac{4\pi}{|\mathbf{G}-\mathbf{k}+\mathbf{k}'|^2}\, \mathcal{Y}_{i\mathbf{k},j\mathbf{k}'}(\mathbf{G})\, \mathcal{Y}_{j\mathbf{k}',i\mathbf{k}}(-\mathbf{G}), \tag{18}$$

where $\mathcal{Y}_{i\mathbf{k},j\mathbf{k}'}(\mathbf{G})$ are the Fourier transforms of the codensities $\psi^*_{i\mathbf{k}}(\mathbf{r})\psi_{j\mathbf{k}'}(\mathbf{r})$,

$$\mathcal{Y}_{i\mathbf{k},j\mathbf{k}'}(\mathbf{G}) = \int_\Omega e^{-i(\mathbf{G}-\mathbf{k}+\mathbf{k}')\cdot\mathbf{r}}\, \psi^*_{i\mathbf{k}}(\mathbf{r})\, \psi_{j\mathbf{k}'}(\mathbf{r})\, \mathrm{d}\mathbf{r}, \tag{19}$$

and the $\mathbf{G} = \mathbf{k} - \mathbf{k}'$ Coulomb singularity is regularised by the Gygi-Baldereschi prescription [26]. As noted above, $E_{\rm xc}$ is evaluated through ACE.

### C. Iterative minimization

For a fixed $N$ electrons, the energy solution can be found by minimizing the objective function $E$

$$E_{\rm gs} = \min_{\{\mathsf{n}_\mathbf{k}\},\,\{\mathsf{C}_\mathbf{k}\}} E[\{\mathsf{n}_\mathbf{k}\},\{\mathsf{C}_\mathbf{k}\}] \tag{20}$$

subject to the N-representability constraints Eq. (8) and the orthogonality constraint Eq. (12), namely,

$$\begin{cases} \displaystyle\sum_{i\mathbf{k}} w_{\mathbf{k}} n_{i\mathbf{k}} - N_e = 0, \\ \quad 0 \le n_{i\mathbf{k}} \le 1, \\ (\mathsf{C}_\mathbf{k})^\dagger \mathsf{S}_\mathbf{k} \mathsf{C}_\mathbf{k} - \mathsf{I}_{N_{\rm b}} = 0. \end{cases} \tag{21}$$

for all $\mathbf{k}$. The objective function is

$$E[\gamma] \;=\; \sum_{i\mathbf{k}} w_{\mathbf{k}} n_{i\mathbf{k}} \int \mathrm{d}\mathbf{r}\, \psi^*_{i\mathbf{k}}(\mathbf{r}) h_\mathbf{k} \psi_{i\mathbf{k}}(\mathbf{r}) + \frac{1}{2}\iint d\mathbf{r}\, d\mathbf{r}' \frac{\rho(\mathbf{r})\rho(\mathbf{r}')}{|\mathbf{r}-\mathbf{r}'|} + E_{\rm xc}[\gamma], \tag{22}$$

where one-body Hamiltonian $h_\mathbf{k} = T_\mathbf{k} + V^{\rm loc}_\mathbf{k} + V^{\rm nl}_\mathbf{k}$ collects kinetic, local pseudopotential, and nonlocal pseudopotential contributions in the usual Kohn-Sham sense, and $E_{\rm xc}[\gamma]$ is given by Eq. (16) with separable kernels as in Eq. (17).

The solution of the minimization problem gives the ground-state 1-RDM $\gamma_{\rm gs}$ in the spectral representation. To find the solution, we adopt the iterative minimization approach by updating the occupation numbers and the orbital coefficients in an alternating fashion in each iteration. This approach requires the gradient of the objective function with respect to the occupation numbers and the orbital coefficients,

$$\nabla_{\mathsf{n}_\mathbf{k}} E(\{\mathsf{n}_\mathbf{k}\},\{\mathsf{C}_\mathbf{k}\}), \quad \text{and} \quad \nabla_{\mathsf{C}_\mathbf{k}} E(\{\mathsf{n}_\mathbf{k}\},\{\mathsf{C}_\mathbf{k}\}). \tag{23}$$

#### *1. Occupation number optimization*

The occupation numbers obey two constraints in Eq. (8). One is the electron-number constraint, and the other is box constraint. Previously for the box constraint, the constrained optimization problem is converted into an unconstrained problem, by introducing a parameterization function. Two commonly used functions are the cosine square function $\cos^2\theta$ and the sigmoid function $\frac{1}{1+e^{-x}}$.

The electron-number constraint can then be handled by using a Lagrangian multiplier. An improved treatment is to add a quadratic penalty term to the objective function, which is known as the augmented Lagrangian method. With $c(\mathsf{n}) = \sum_{i\mathbf{k}} w_\mathbf{k} n_{i\mathbf{k}} - N_e$, the ALM objective function $E_{\rm ALM}$ is

$$E_{\rm ALM}(\mathsf{n},\lambda,\mu) = E(\mathsf{n}) + \lambda c(\mathsf{n}) + \frac{\mu}{2} c(\mathsf{n})^2, \tag{24}$$

where parameters $\lambda$ and $\mu$ are parameters to be determined. The Lagrange multiplier are updated, $\lambda \leftarrow \lambda + \mu\, c(\mathsf{n})$, based on the Karush-Kuhn-Tucker (KKT) optimality conditions [27], while the penalty parameter $\mu$ is adjusted heuristically to improve convergence, e.g. $\mu$ may be increased by a factor about 2-5 if $|c|$ remains large. This ALM method typically requires large number of iterations to converge and is less optimal when evaluation of the objective

function is expensive. The electron-number constraint is also only approximately achieved when convergence is reached.

The earliest implementation for solid is probably in the LAPW code ELK by Sharma et al. [14]. There, the occupation numbers are optimised directly in $\mathsf{n}$-space on a straight, box-respecting segment that preserves the electron count exactly. Recently, the usage of EBI map for the molecular systems has been proposed by Yao *et al.* [28, 29]. EBI replaces the box-constrained vector $\mathsf{n}$ by unconstrained parameters $\mathsf{x}$ and a scalar parameter $\mu$ that enforces the electron count implicitly. Instead of using the Newton's method, we choose to use the gradient-based method, which only needs the first-order gradient. Per band $i$ and point $\mathbf{k}$,

$$n_{i\mathbf{k}} = \tfrac{\mathrm{erf}(x_{i\mathbf{k}}+\mu)+1}{2}, \tag{25}$$

with $\mu$ found by bisection on $\zeta(\mu) = \sum_{i\mathbf{k}} w_{\mathbf{k}} n_{i\mathbf{k}} - N_e = 0$. Writing $u_{i\mathbf{k}} \equiv x_{i\mathbf{k}} + \mu$, the chain rule gives

$$\frac{\partial n_{i\mathbf{k}}}{\partial u_{i\mathbf{k}}} = \tfrac{1}{2}\,\mathrm{erf}'(u_{i\mathbf{k}}) = \frac{1}{\sqrt{\pi}}\, e^{-u_{i\mathbf{k}}^2}, \tag{26}$$

using $\mathrm{erf}'(x) = \frac{2}{\sqrt{\pi}} e^{-x^2}$. Following the EBI supplementary derivation [28], $\mu$ is an implicit function of $\mathsf{x}$ fixed by the electron-count constraint $\zeta(\mathsf{x}, \mu) = \sum_{i\mathbf{k}} w_{\mathbf{k}} n_{i\mathbf{k}} - N_e = 0$. For any fixed $\mathsf{x}$, $\zeta$ is strictly monotone in $\mu$ because $\partial n_{i\mathbf{k}}/\partial u_{i\mathbf{k}} > 0$ and $w_{\mathbf{k}} > 0$, so a unique root $\mu(\mathsf{x})$ exists. Differentiating $\zeta(\mathsf{x}, \mu(\mathsf{x})) = 0$ with respect to $x_{i\mathbf{k}}$ then gives

$$\sum_{j\mathbf{k}'} w_{\mathbf{k}'}\, \frac{\partial n_{j\mathbf{k}'}}{\partial x_{i\mathbf{k}}} = 0. \tag{27}$$

With $u_{j\mathbf{k}'} = x_{j\mathbf{k}'} + \mu$ and the chain rule,

$$\frac{\partial n_{j\mathbf{k}'}}{\partial x_{i\mathbf{k}}} = \frac{\partial n_{j\mathbf{k}'}}{\partial u_{j\mathbf{k}'}} \left( \delta_{ij}\delta_{\mathbf{k}\mathbf{k}'} + \frac{\partial \mu}{\partial x_{i\mathbf{k}}} \right), \tag{28}$$

Eq. (27) becomes

$$w_{\mathbf{k}} \frac{\partial n_{i\mathbf{k}}}{\partial u_{i\mathbf{k}}} + \frac{\partial \mu}{\partial x_{i\mathbf{k}}} \sum_{j\mathbf{k}'} w_{\mathbf{k}'} \frac{\partial n_{j\mathbf{k}'}}{\partial u_{j\mathbf{k}'}} = 0, \qquad \text{hence} \qquad \frac{\partial \mu}{\partial x_{i\mathbf{k}}} = -\frac{w_{\mathbf{k}} \frac{\partial n_{i\mathbf{k}}}{\partial u_{i\mathbf{k}}}}{\sum_{j\mathbf{k}'} w_{\mathbf{k}'} \frac{\partial n_{j\mathbf{k}'}}{\partial u_{j\mathbf{k}'}}}, \tag{29}$$

where the denominator is $\partial\zeta/\partial\mu \neq 0$. (In the molecular EBI formulae the Brillouin-zone weights are unity and the sums run over orbitals only [28, 29].) With the occupation gradient $g_{i\mathbf{k}} = \partial E/\partial n_{i\mathbf{k}}$, the gradient with respect to $x_{i\mathbf{k}}$ follows from the chain rule $\partial E/\partial x_{i\mathbf{k}} = \sum_{j\mathbf{k}'} g_{j\mathbf{k}'}\, \partial n_{j\mathbf{k}'}/\partial x_{i\mathbf{k}}$, which leads to

$$\frac{\partial E}{\partial x_{i\mathbf{k}}} = \frac{\partial n_{i\mathbf{k}}}{\partial u_{i\mathbf{k}}} \left( g_{i\mathbf{k}} - w_{\mathbf{k}}\, R \right), \qquad R \equiv \frac{\sum_{j\mathbf{k}'} w_{\mathbf{k}'}\, g_{j\mathbf{k}'} \frac{\partial n_{j\mathbf{k}'}}{\partial u_{j\mathbf{k}'}}}{\sum_{j\mathbf{k}'} w_{\mathbf{k}'} \frac{\partial n_{j\mathbf{k}'}}{\partial u_{j\mathbf{k}'}}}. \tag{30}$$

The variable $x_{i\mathbf{k}}$ is updated with $x_{i\mathbf{k}} \leftarrow x_{i\mathbf{k}} - \tau \frac{\partial E}{\partial x_{i\mathbf{k}}}$ where step size of $\tau$ is found by a simple backtracking Armijo line search.

In this work, we minimize $E(\mathsf{n})$ at fixed natural orbitals using the spectral projected gradient method (SPG) of Birgin *et al.* [30]. For a periodic solid, every trial occupation vector must satisfy the box bounds $0 \le n_{i\mathbf{k}} \le 1$ and the BZ-weighted electron-count constraint $\sum_{i\mathbf{k}} w_{\mathbf{k}} n_{i\mathbf{k}} = N_e$. We collect all such vectors in the set

$$\Omega = \Big\{ \mathsf{n} :\ 0 \le n_{i\mathbf{k}} \le 1,\ \sum_{i\mathbf{k}} w_{\mathbf{k}} n_{i\mathbf{k}} = N_e \Big\}. \tag{31}$$

Whenever a trial vector $\mathsf{x}$ violates these constraints, SPG first maps it back to an allowable $\mathsf{n} \in \Omega$ by a projection step [31]

$$P_w(x_{i\mathbf{k}}) = \mathrm{clip}\big(x_{i\mathbf{k}} - \lambda\, w_{\mathbf{k}},\, 0,\, 1\big), \tag{32}$$

where $\mathrm{clip}(y, 0, 1)$ truncates $y$ to $[0, 1]$. The scalar $\lambda$ is fixed by bisection on the monotone, piecewise-linear function

$$G(\lambda) \equiv \sum_{i\mathbf{k}} w_{\mathbf{k}}\, P_w(x_{i\mathbf{k}}) - N_e = 0, \tag{33}$$

so that the projected occupations sum to $N_e$. The coefficient $\lambda w_{\mathbf{k}}$ in Eq. (32) makes $P_w(\mathsf{x})$ the allowable occupation vector closest to $\mathsf{x}$, in the sense of minimizing $\sum_{i\mathbf{k}}(n_{i\mathbf{k}} - x_{i\mathbf{k}})^2$ over $\mathsf{n} \in \Omega$. Appendix A derives Eq. (32) and Eq. (33) and verifies compatibility with SPG [30].

At $\mathsf{n}_0 \in \Omega$, the energy gradient $\mathsf{g} = \nabla_{\mathsf{n}} E$ has components $g_{i\mathbf{k}} = \partial E/\partial n_{i\mathbf{k}}$. To decide whether the inner loop has converged, SPG uses the projected-gradient map of Birgin *et al.* [30]

$$\mathsf{g}_t(\mathsf{n}) \equiv P_w(\mathsf{n} - t\,\mathsf{g}) - \mathsf{n}, \qquad t > 0, \tag{34}$$

which measures how much a raw gradient step of size $t$ must be corrected to restore the constraints. When $t = 1$, a small value of $\|\mathsf{g}_1(\mathsf{n}_0)\|_\infty$ signals that $\mathsf{n}_0$ is close to a constrained minimum and no further update is needed, where $\|\cdot\|_\infty$ denotes the infinity norm (or the maximum norm).

Otherwise one SPG inner iteration proceeds as follows; the integer $k$ labels the iteration ($k = 1, 2, \ldots$) and is distinct from the Bloch vector $\mathbf{k}$. An adaptive Barzilai-Borwein spectral steplength $\alpha_k$ is taken from the two most recent accepted iterations [30, 32]; on the first step $\alpha_k = 1/\|\mathsf{g}_1(\mathsf{n}_0)\|_\infty$. The algorithm forms a *feasible chord*: it takes a gradient step, projects back to $\Omega$, and connects the endpoints by a straight line (see Fig. 1),

$$\mathsf{d}_k = \mathsf{g}_{\alpha_k}(\mathsf{n}_0) = P_w(\mathsf{n}_0 - \alpha_k \mathsf{g}) - \mathsf{n}_0, \qquad \mathsf{n}(\lambda) = \mathsf{n}_0 + \lambda\,\mathsf{d}_k, \quad \lambda \in [0, 1]. \tag{35}$$

Because both $\mathsf{n}_0$ and $\mathsf{n}_0 + \mathsf{d}_k$ lie in $\Omega$, every $\lambda \in [0, 1]$ obeys the box and electron-count constraints exactly, as

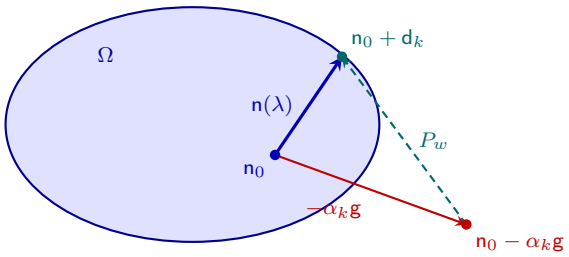


FIG. 1. Schematic of one SPG occupation step. From $\mathsf{n}_0 \in \Omega$ near the feasible boundary, a spectral gradient step $-\alpha_k \mathsf{g}$ (red) may leave $\Omega$; the projector $P_w$ (teal) returns the trial to $\mathsf{n}_0 + \mathsf{d}_k \in \Omega$. The search then follows the feasible chord $\mathsf{n}(\lambda) = \mathsf{n}_0 + \lambda \mathsf{d}_k$ (blue), $\lambda \in [0, 1]$.

schematically illustrated in Fig. 1. The energy $E(\lambda) \equiv E(\mathsf{n}(\lambda))$ is then reduced along this chord, starting from $\lambda_0 = 1$.

A trial $\lambda$ is accepted when it satisfies the Armijo sufficient-decrease test [30, 33, 34],

$$E(\lambda) \le f_{\max} + \gamma\,\lambda\,\phi'(0), \qquad \phi'(0) = \mathsf{g}^\top \mathsf{d}_k, \tag{36}$$

where $\phi'(0)$ is the initial energy derivative along the chord ($\lambda = 0$), $\gamma > 0$, and $f_{\max} = \max\{E(\mathsf{n}^{(k-j)}) \mid 0 \le j \le \min\{k, M-1\}\}$; $\mathsf{n}^{(k-j)}$ denotes the occupation vector at inner iteration $k - j$. For $M > 1$ this is the Grippo-Lampariello-Lucidi nonmonotone rule [34], which can help the optimizer cross shallow barriers; for $M = 1$ only $j = 0$ enters and $f_{\max} = E(\mathsf{n}_0)$, reducing Eq. (36) to the usual monotone Armijo condition [33]. In this work, we have set $M = 1$ for the monotone Armijo condition. If a trial with $\lambda > 1$ leaves $\Omega$, it is repaired by $P_w$.

### 2. *Orbital optimization on generalized Stiefel manifolds*

For the orbital sub-problem with fixed occupations, the orbital coefficients are constrained by Eq. (12), so Euclidean updates must be replaced by geometry-aware steps. Following our previous work [21], natural orbital coefficients in a given basis live on the generalized Stiefel manifold,

$$\mathrm{St}(N_b, N_{\mathrm{basis}}; \mathsf{S}) = \left\{\mathsf{X} \in \mathbb{C}^{N_{\mathrm{basis}} \times N_b} : \mathsf{X}^\dagger \mathsf{S} \mathsf{X} = \mathsf{I}_{N_b}\right\}, \tag{37}$$

with $N_{\mathrm{basis}}$ the number of basis functions per band. For planewave calculations with norm-conserving pseudopotentials, the overlap matrix is the identity, $\mathsf{S} = \mathsf{I}_{N_{\mathrm{basis}}}$. More generally, for $N_{\mathrm{ao}}$ atomic orbital (AO) basis functions, by applying a Cholesky factorization of $\mathsf{S}$, the generalized Stiefel manifold $\mathrm{St}(N_b, N_{\mathrm{ao}}; \mathsf{S})$ can be mapped to the standard Stiefel manifold. At $\mathsf{X} \in \mathrm{St}(N_b, N_{\mathrm{basis}}; \mathsf{I}_{N_{\mathrm{basis}}})$, we have the tangent space

$$T_{\mathsf{X}}\mathrm{St} = \left\{\mathsf{Y} = \mathsf{X}\mathsf{B} + \mathsf{Z} \mid \mathsf{B}^\dagger = -\mathsf{B},\ \mathsf{Z}^\dagger \mathsf{X} = 0\right\}, \tag{38}$$

where $\mathsf{Y}, \mathsf{Z} \in \mathbb{C}^{N_{\text{basis}} \times N_b}$, $\mathsf{B} \in \mathbb{C}^{N_b \times N_b}$. Here, $\mathsf{B}$ is a skew-Hermitian matrix and $\mathsf{Z}$ is a matrix orthogonal to $\mathsf{X}$. For the Stiefel manifold, the canonical metric is used

$$\langle \mathsf{U}, \mathsf{V} \rangle_{\mathsf{X}}^{c} = \operatorname{tr}\left[ \mathsf{U}^{\dagger} \left( \mathsf{I}_{N_{\text{basis}}} - \frac{1}{2} \mathsf{X}\mathsf{X}^{\dagger} \right) \mathsf{V} \right] \tag{39}$$

where $\mathsf{U}, \mathsf{V} \in T_{\mathsf{X}}\mathrm{St}$. The orthogonal projection of any vector $\mathsf{V} \in \mathbb{C}^{N_{\text{basis}} \times N_b}$ onto $T_{\mathsf{X}}\mathrm{St}$ is

$$\pi_{\mathsf{X}}(\mathsf{V}) = \mathsf{V} - \mathsf{X}\,\mathrm{sym}(\mathsf{X}^{\dagger}\mathsf{V}) \quad \text{with} \quad \mathrm{sym}(A) = \tfrac{1}{2}(A + A^{\dagger}). \tag{40}$$

Two essential components of retraction and vector transport are needed in the Riemannian optimization (see details in [21]). In this work, we used the polar decomposition as the retraction and the vector transport by projection as the vector transport. For multiple-k points, the coefficients are stored using the product of Stiefel manifolds as done in [21],

$$\prod_{\mathbf{k}=1}^{N_{\text{k}}} \mathrm{St}(N_b, N_{\text{basis}}; \mathsf{I}_{N_{\text{basis}}}). \tag{41}$$

The Euclidean gradient in the ambient coefficient space is $\nabla E$ (its argument of $\mathsf{C}_{\mathbf{k}}$ is omitted for simplicity) the corresponding Riemannian gradient $\mathsf{g} = \operatorname{grad} E$ in the Stiefel manifold, can be computed with the Euclidean gradient

$$\operatorname{grad} E = \nabla E - \mathsf{X}\,(\nabla E)^{\dagger}\,\mathsf{X}. \tag{42}$$

In the conjugate gradient method, the new search direction $\mathsf{d}_{k+1}$ is computed as

$$\mathsf{d}_{k+1} = -\mathsf{g}_{k+1} + \beta_{k+1} \mathcal{T}_{\alpha_k \mathsf{d}_k}(\mathsf{d}_k), \tag{43}$$

where $\mathcal{T}_{\alpha_k \mathsf{d}_k}(\mathsf{d}_k)$ is the projection based vector transport. Again, we used the Polak-Ribière form for the $\beta$ parameter in the conjugate gradient method.

Combining these two optimization strategies, our RDMFT algorithm can be illustrated in Fig. 2. Such algorithmic design allows easy substitution of alternative methods, e.g. in the occupation part the SPG method can be replaced with the EBI method. The outer maximum iteration $K_{\text{out}}$ and the inner maximum iterations $K_{\text{occ}}$ and $K_{\text{orb}}$ are used to control the number of alternating outer cycles and the effort spent in each occupation and orbital subproblem, respectively. Besides the energy tolerance $\epsilon_{\text{E}}$ for the outer loop, the gradient tolerances $\epsilon_{\text{orb}}$ and $\epsilon_{\text{occ}}$ set the convergence thresholds for the orbital and occupation subproblems, respectively. Post-processing of the natural occupations and the natural orbitals can be done after the convergence has been reached; further observables are discussed in Sec. V.

## III. IMPLEMENTATION AND COMPUTATIONAL DETAILS

The algorithms of Sec. II C, with occupation updates in Sec. II C 1 and orbital updates in Sec. II C 2, are realized in the planewave QE package version 7.5 as a self-consistent-field variational minimization[20]. After a converged Kohn-Sham or hybrid calculation, the solver updates the natural occupations $n_{i\mathbf{k}} \in [0, 1]$ and the natural orbitals $\psi_{i\mathbf{k}}(\mathbf{r})$ already stored as planewave coefficient matrices. The energy is iteratively minimized subject to Eq. (8) and the orthonormality constraint of Eq. (12). The initial occupation numbers are seeded from a KS calculation using the smearing method to start with Fermi-Dirac initial guess. The initial orbital coefficients can be seeded from a few-step KS calculation such that initial orbitals are orthonormalized. Given the minimal cost of KS calculation, starting with a converged set of KS orbitals is recommended as the kinetic energy has been largely suppressed.

To make sure that the implementation is correct, the analytical derivatives with respect to the occupation numbers and the orbital coefficients are calculated and compared with the finite difference method to a very high accuracy. The consistency between the objective function and its gradients is also crucial for the line search to work properly.

All the calculations are performed using the modified planewave QE package as noted above. Natural orbitals are all expanded in the planewave basis with an energy cutoff of 70 Ry. The norm-conserving pseudopotentials (ONCV) [35] are used to describe the electron-ion interactions. For molecules and other isolated systems, only the $\Gamma$ point is used in a cubic supercell of length 15.0 Å. For charged systems, the spin-polarized calculation is needed and the Martyna-Tuckerman correction is applied [36]. For power-functionals, the exponent is set to $\alpha = 0.65$. Benchmark solid calculations only uses Monkhorst-Pack k-point meshes of $2 \times 2 \times 2$ unless stated otherwise. For the Fock operator sampling, we use $2 \times 2 \times 2$ q-grid. The Coulomb potential divergences at small q vectors are treated using the Gygi-Baldereschi correction [26]. The ACE algorithm is used in the construction of the EXX. All the calculations stop

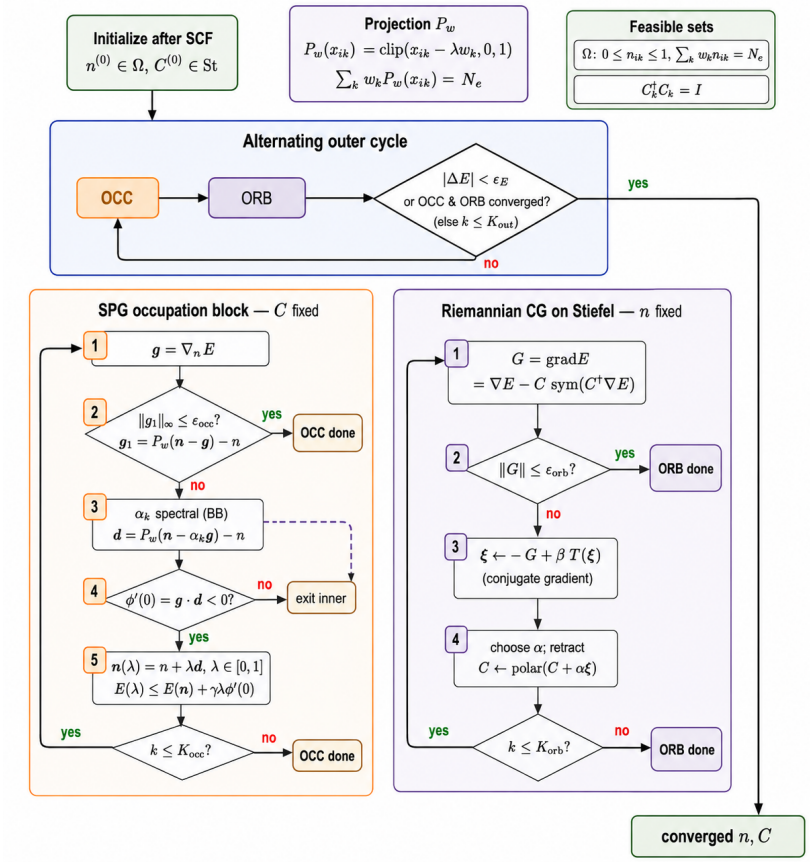


FIG. 2. Schematic illustration of the RDMFT algorithm with the SPG occupation optimizer and the Riemannian conjugate gradient orbital optimizer.

when the energy difference between two consecutive iterations is less than $10^{-8}$ Ry. Unless stated otherwise, Sec. IV uses the settings above with the following additions: HF and power functional benchmarks on $H_2$, Si, and Na employ a $2 \times 2 \times 2$ Monkhorst-Pack mesh with offset $(0.215, 0.35, 0.625)$. Occupations and orbitals are optimized alternately except for the test of initial occupation where orbitals are frozen at converged HF values. RDMFT runs are capped at 50 outer iterations where noted and by default maximum 10 inner iterations is set for both the orbital and the occupation loop.

## IV. RESULTS AND DISCUSSION

### A. Implementation validation

We first verify the RDMFT implementation against HF references from converged Kohn-Sham hybrid calculations on three representative systems: an isolated $H_2$ molecule, gapped silicon bulk (cubic diamond), and metallic sodium bulk (body-centered cubic). Computational parameters follow Sec. III; the $H_2$ equilibrium bond length is 0.7414 Å, Si uses a two-atom primitive cell with conventional cubic lattice constant $a = 10.236$ a.u. ($a/2 = 5.118$ a.u.), and Na a one-atom primitive cell with cubic lattice constant $a = 8.108$ a.u.

For RDMFT, we compare the SPG and EBI occupation optimizers with the same Riemannian conjugate-gradient orbital update. To depart from the idempotent KS starting point, initial occupations are obtained by Gaussian smearing with width 0.1 Ry. Total energies are listed in Table II and occupations in Table III.

For $H_2$, SPG reproduces the HF energy and occupations exactly ($\Delta E = 0$). EBI agrees to within $0.12\,\mu$Ry while preserving the occupied occupations. For silicon, SPG again matches the KS reference exactly ($\Delta E = 0$). EBI stops short of full convergence ($\Delta E = +0.71\,$mRy) and slightly undershoots valence occupations (e.g. 0.9997 instead of 1.0 on several bands) while populating conduction states at the $10^{-4}$ level. For sodium, SPG remains accurate to $0.01\,\mu$Ry and reproduces the KS occupations exactly, including the 0.5 occupation at the Fermi level. EBI gives

$\Delta E = +0.11\,\mathrm{mRy}$ and shifts the Fermi-level occupation to 0.4998 while introducing a small occupation ($2.4 \times 10^{-4}$) on an adjacent band.

Overall, SPG is the more reliable choice for these HF benchmarks across molecules, gapped solids, and metals. When occupations approach 0 or 1, the erf parameterization used in EBI (Sec. II C 1) suppresses occupation updates through vanishing derivatives, whereas SPG projects directly onto the feasible set and avoids this issue. Occupation parameterizations can also create artificial saddle points when occupations are degenerate [37], typically requiring a second-order treatment to escape them. Because SPG does not introduce an auxiliary parameterization, it is not subject to this mechanism; across the systems tested here we observe no such trapping, though a broader assessment remains warranted.

TABLE II. Total energies from Kohn-Sham hybrid SCF and RDMFT with the HF functional. Values in parentheses give $\Delta E = E_{\mathrm{RDMFT}} - E_{\mathrm{KS}}$ in $\mu$Ry or mRy, as indicated. $^{\dagger}$ marks EBI runs that did not reach the $10^{-8}$ Ry convergence threshold.

| System | KS | SPG | EBI |
|---|---|---|---|
| $H_2$ | $-2.26575897$ | $-2.26575897\,(+0\,\mu\mathrm{Ry})$ | $-2.26575885\,(+0.12\,\mu\mathrm{Ry})$ |
| Si | $-15.07589955$ | $-15.07589955\,(+0\,\mu\mathrm{Ry})$ | $-15.07518854^{\dagger}\,(+0.71\,\mathrm{mRy})$ |
| Na | $-84.49001110$ | $-84.49001109\,(+0.01\,\mu\mathrm{Ry})$ | $-84.48990456^{\dagger}\,(+0.11\,\mathrm{mRy})$ |

TABLE III. HF occupations for $H_2$, Si, and Na. $i_k$ and $i_b$ are the $k$-point and band indices, respectively. EBI deviations concentrate near the Fermi level for Si and Na.

| $i_k$ | $i_b$ | $H_2$ | | | Si | | | Na | | |
|---|---|---|---|---|---|---|---|---|---|---|
| | | KS | SPG | EBI | KS | SPG | EBI | KS | SPG | EBI |
| 1 | 1 | 1.000000 | 1.000000 | 1.000000 | 1.000000 | 1.000000 | 1.000000 | 1.000000 | 1.000000 | 1.000000 |
| 1 | 2 | 0.000000 | 0.000000 | 0.000000 | 1.000000 | 1.000000 | 0.999665 | 1.000000 | 1.000000 | 1.000000 |
| 1 | 3 | 0.000000 | 0.000000 | 0.000000 | 1.000000 | 1.000000 | 0.999665 | 1.000000 | 1.000000 | 1.000000 |
| 1 | 4 | 0.000000 | 0.000000 | 0.000000 | 1.000000 | 1.000000 | 0.999665 | 1.000000 | 1.000000 | 1.000000 |
| 1 | 5 | | 0.000000 | 0.000000 | 0.000000 | 0.000000 | 0.000144 | 1.000000 | 1.000000 | 0.999778 |
| 1 | 6 | | | | 0.000000 | 0.000000 | 0.000144 | 0.000000 | 0.000000 | 0.000000 |
| 1 | 7 | | | | 0.000000 | 0.000000 | 0.000144 | 0.000000 | 0.000000 | 0.000000 |
| 1 | 8 | | | | 0.000000 | 0.000000 | 0.000068 | 0.000000 | 0.000000 | 0.000000 |
| 1 | 9 | | | | | | | 0.000000 | 0.000000 | 0.000000 |
| 2 | 1 | | | | 1.000000 | 1.000000 | 1.000000 | 1.000000 | 1.000000 | 1.000000 |
| 2 | 2 | | | | 1.000000 | 1.000000 | 1.000000 | 1.000000 | 1.000000 | 1.000000 |
| 2 | 3 | | | | 1.000000 | 1.000000 | 0.999769 | 1.000000 | 1.000000 | 1.000000 |
| 2 | 4 | | | | 1.000000 | 1.000000 | 0.999769 | 1.000000 | 1.000000 | 1.000000 |
| 2 | 5 | | | | 0.000000 | 0.000000 | 0.000193 | 0.500000 | 0.500000 | 0.499794 |
| 2 | 6 | | | | 0.000000 | 0.000000 | 0.000087 | 0.000000 | 0.000000 | 0.000243 |
| 2 | 7 | | | | 0.000000 | 0.000000 | 0.000087 | 0.000000 | 0.000000 | 0.000000 |
| 2 | 8 | | | | 0.000000 | 0.000000 | 0.000000 | 0.000000 | 0.000000 | 0.000000 |
| 2 | 9 | | | | | | | 0.000000 | 0.000000 | 0.000000 |
| 3 | 1 | | | | 1.000000 | 1.000000 | 1.000000 | 1.000000 | 1.000000 | 1.000000 |
| 3 | 2 | | | | 1.000000 | 1.000000 | 1.000000 | 1.000000 | 1.000000 | 1.000000 |
| 3 | 3 | | | | 1.000000 | 1.000000 | 0.999868 | 1.000000 | 1.000000 | 1.000000 |
| 3 | 4 | | | | 1.000000 | 1.000000 | 0.999868 | 1.000000 | 1.000000 | 1.000000 |
| 3 | 5 | | | | 0.000000 | 0.000000 | 0.000279 | 0.000000 | 0.000000 | 0.000000 |
| 3 | 6 | | | | 0.000000 | 0.000000 | 0.000279 | 0.000000 | 0.000000 | 0.000000 |
| 3 | 7 | | | | 0.000000 | 0.000000 | 0.000000 | 0.000000 | 0.000000 | 0.000000 |
| 3 | 8 | | | | 0.000000 | 0.000000 | 0.000000 | 0.000000 | 0.000000 | 0.000000 |
| 3 | 9 | | | | | | | 0.000000 | 0.000000 | 0.000000 |

We next compare SPG and EBI with the power functional on the same three systems. Table IV lists the RDMFT total energies after up to 50 outer iterations. SPG yields lower energies than EBI for all three systems. After 50 outer iterations, EBI has not reached the $10^{-8}$ Ry threshold for Si and Na; SPG also remains above threshold for Na but is already lower in energy than EBI. Figure 3 shows the energy as a function of outer iteration, using the lower of the two optimizer energies as reference. SPG converges monotonically to the lower values, whereas EBI stagnates at higher energy and is unlikely to converge to the lower plateau even with larger outer iterations.

To test sensitivity to the starting occupations, we apply a controlled perturbation $\epsilon$ to bands near the Fermi level: occupations below 0.5 are increased by $\epsilon$ and those above 0.5 are decreased by $\epsilon$. Initial orbitals are taken from a converged HF calculation and held fixed to isolate occupation optimization. Using the power functional on bulk Na,

TABLE IV. RDMFT total energies with the power functional. † denotes runs that reached 50 outer iterations without meeting the $10^{-8}$ Ry convergence criterion.

| System | SPG | EBI |
|---|---|---|
| $H_2$ | −2.26891386 | −2.26575948 |
| Si | −15.19544633 | −15.18957380† |
| Na | −84.61019266† | −84.59587115† |

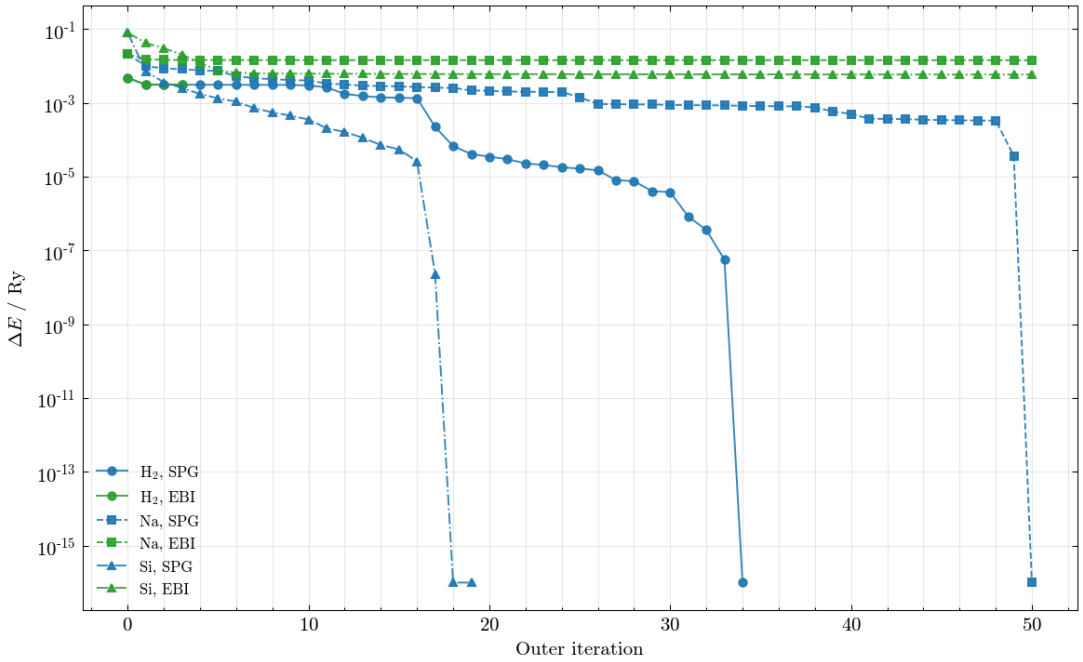


FIG. 3. Energy convergence for the power functional with SPG and EBI occupation optimizers. The reference energy is the lower value between the two optimizers at each system.

we vary $\epsilon$ from $10^{-4}$ to $10^{-1}$ for both SPG and EBI. For occupation optimization only, SPG returns the same energy within ∼70 inner iterations for all perturbation strengths, whereas EBI yields distinct, non-converged energies after 500 inner iterations.

### B. Molecules

The same RDMFT formulation developed above applies without change to isolated molecules and to periodic solids. We compare fractionally charged LiH with published RDMFT data [14]. Here the total electron number is varied through a charge parameter $\delta$ (equivalently $N_e = 4+\delta$ for LiH). Quantitative agreement with the hybrid KS reference for this charged molecule requires a spin-polarized treatment together with the Martyna–Tuckerman correction for electrostatic finite-size effects [36] (Sec. III); the planewave cutoff is 70 Ry. RDMFT is then iterated until the energy criterion of Sec. III is met.

As a reference, we first reproduce the standard HF curve. Published results of Sharma *et al.* [14] are digitized for comparison. Because all-electron and pseudopotential calculations differ in absolute energy, all curves are shifted by subtracting the neutral HF energy $E^{\mathrm{HF}}_{\delta=0}$. Figure 4 shows that our HF results (SPG occupation optimizer) agree with the KS reference to within numerical precision and display the expected piecewise concave shape [38, 39]. The digitized Sharma data lie slightly above this reference, which is indicative of incomplete convergence.

With the power functional, our RDMFT energies largely agree with Sharma *et al.* [14] and are slightly lower at several charge points. For the Müller functional, our converged curve lies substantially below the published data; the largest difference at $N_e = 5.0$ ($\delta = 1.0$) is about 0.1 Ha. Müller converges more slowly than the power functional in these runs, and the huge discrepancy is again likely due to their failure in achieving convergence. Further investigation is needed to figure out the exact reason and is left for future. These comparisons show that the present SPG-based

algorithm converges more reliably and to lower energies than the earlier solid-state RDMFT data for fractionally charged LiH, and thereby provides a more trustworthy platform for studying the derivative discontinuity and for probing convexity or concavity of the underlying XC functional.

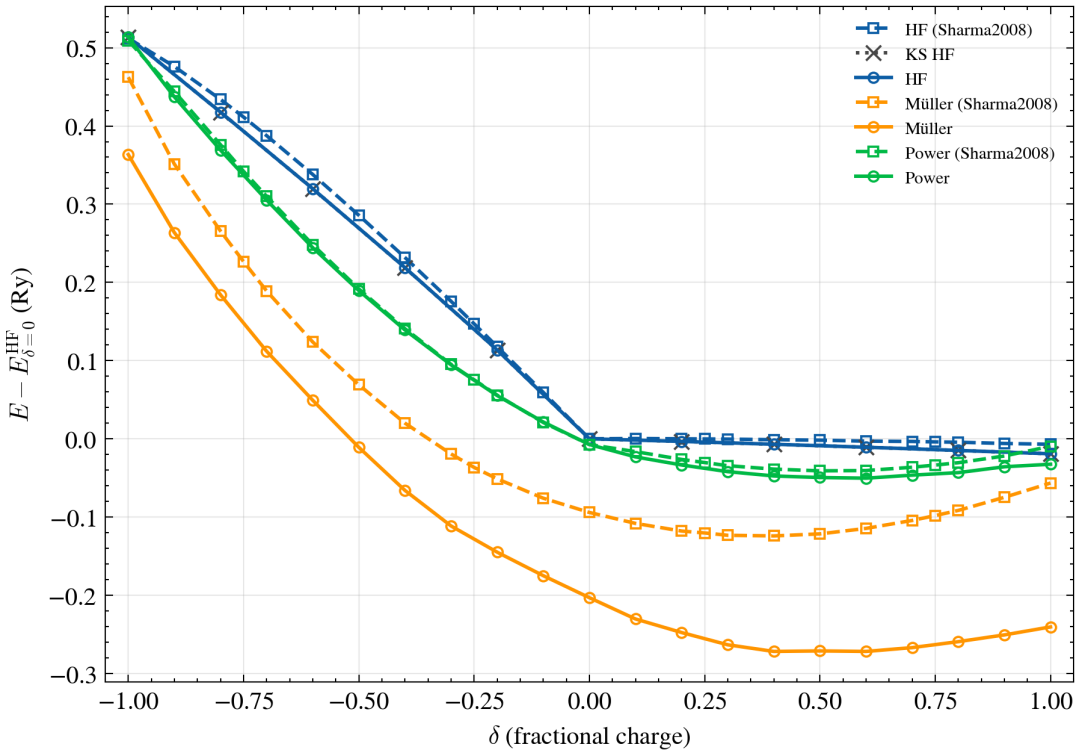


FIG. 4. Fractionally charged LiH: RDMFT total energies relative to $E^{\mathrm{HF}}_{\delta=0}$. Black: HF reference using KS hybrid loop; blue: present HF (SPG); green: power functional (SPG); orange: Müller functional (SPG). Dashed curves: digitized data from Sharma *et al.* [14].

Bond dissociation provides a stringent test of RDMFT because the correct description requires fractional natural occupations on the dissociation limit. Figure 5 compares the total energy curves of PBE [40] in DFT, power and Müller functional in RDMFT for stretched $H_2$ and $N_2$ against quantum-chemistry references [41], full configuration interaction (full CI) for $H_2$ and multi-configurational self-consistent field (MCSCF) for $N_2$. All calculations are spin-unpolarized. For $H_2$ molecule, the Müller functional yields close dissociation curve compared to HF, PBE, and power functional. However, for the $N_2$ molelcule, Müller gives much lower energies in the dissociation limit, which is consistent with earlier studies [8]. Power functional gives a correct shape but its performance depends on the adopted parameter $\alpha$ for each system. For $H_2$, there are two major natural orbitals whose occupation numbers are far away from boundaries (one strongly occupied and one weakly occupied). RDMFT give both half occupations in the dissociation limit, and the occupation, of either strongly occupied or weakly occupied orbital, of Müller is clearly closer to the half-occupancy than that of power at all bond lengths, which can be regarded as an indicator of stronger correlation. For $N_2$, five such orbitals are involved, their occupations all approach the half occupancy. Again, the occupation of the same band exhibits similar trend as seen in $H_2$.

### C. Solids

We next examine bulk silicon in the diamond structure as a representative solid. To be more realistic, the silicon equation-of-state scans use 4×4×4 with offset $(0.25, 0.25, 0.25)$. Table V summarizes fits from PBE, HF, and PBE0 self-consistent calculations together with RDMFT results for the power and Müller functionals and experimental reference data; Fig. 6 plots the raw energy-volume data. Among the Kohn-Sham references, PBE and HF slightly overestimate the equilibrium lattice constant ($a_0 = 10.37$ and 10.36 a.u., respectively, vs. 10.26 a.u. experimentally), whereas PBE0 is closest to experiment (10.31 a.u.). The present RDMFT power-functional fit gives the same $a_0 = 10.31$ a.u. as PBE0, with $B_0 = 94.5$ GPa and $B_0' = 4.54$, placing the bulk modulus just below the experimental value (97.9 GPa) [42] and

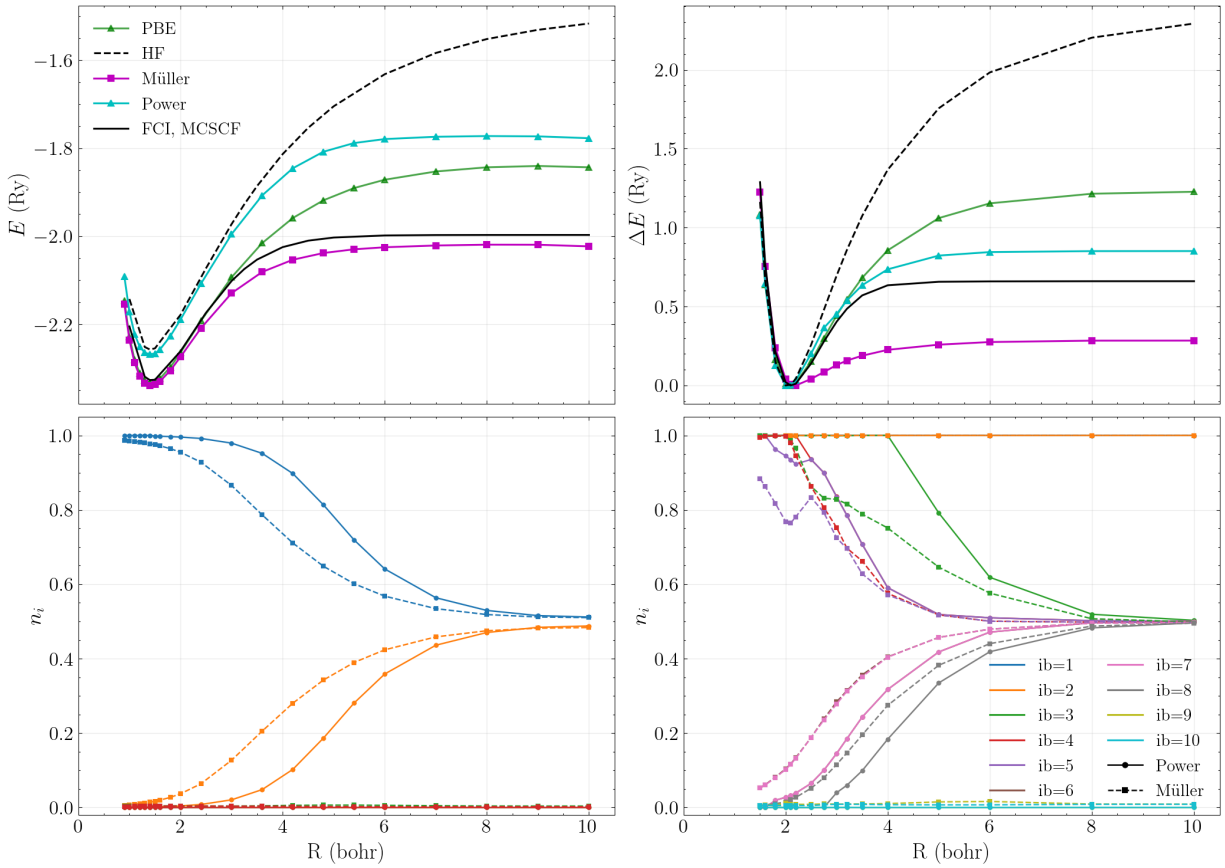


FIG. 5. Dissociation energy curves for $H_2$ and $N_2$ molecules. Full-CI for $H_2$ and MCSCF for $N_2$ are used as references. Dashed black curves are the RHF results [41]. Power functional and Müller functional in RDMFT are presented with the KS PBE results. For $N_2$, the global minimum of each curve is subtracted so that these curves are on the same scale. The natural occupation numbers are shown in the bottom panels for different bond lengths in our RDMFT calculations.

between PBE (86.9 GPa) and HF (105.2 GPa). By contrast, the equilibrium $a_0$ reported by Sharma *et al.* [14] for the power functional with $\alpha = 0.70$ (10.55 a.u.) is expanded by roughly 2.8% relative to experiment. The present Müller fit yields a slightly contracted lattice ($a_0 = 10.20$ a.u.) and a substantially softer $B_0 = 81.2$ GPa with $B_0' = 4.84$, whereas the Sharma *et al.* value (10.49 a.u.) lies on the expanded side of experiment. These trends are visible in Fig. 6, where the Müller curve is shallower near equilibrium than HF or power. Given the huge discrepancy for the Müller curve of LiH molecule, we meticulously converge the calculation for this solid system as we have done for the molecular system. It is likely that the overestimated 10.49 a.u. is an artifact of unconverged calculation instead of the trait of the functional itself. Also Müller functional, well-known for its overcorrelation ought to yield a contracted lattice constant. This is clearly seen in our converged Müller curve with $a_0 = 10.20$ a.u.

Lastly, we have also attempted to calculate a typical transition metal oxide, NiO in the power functional. Our preliminary results show agreement in local moments of 1.38 $\mu_B$ versus reported 1.36 $\mu_B$ in the antiferromagnetic ordering [43]. Further investigation of the spectral properties is underway.

## V. SUMMARY AND OUTLOOK

We have formulated RDMFT for periodic solids in a basis-independent way and implemented it as a planewave post-SCF module in QE that reuses ACE for EXX handling. The solver follows an alternating occupation-orbital strategy with a modular design: occupation and orbital subproblems can be swapped independently. For occupations we adapt spectral projected gradient (SPG) to periodic systems, with Euclidean projection onto the weighted feasible set $\Omega$, and also support first-order EBI with an erf parameterization; for orbitals we use Riemannian conjugate-gradient updates on generalized Stiefel manifolds that enforce natural-orbital orthonormality. Numerical tests show that SPG reliably reproduces HF references on molecules and solids, converges lower with the power functional, and remains insensitive

TABLE V. Third-order Birch-Murnaghan EOS fit parameters for diamond Si. $a_0$ is the conventional eight-atom cubic lattice constant in a.u.; $E_0$ is the equilibrium energy per atom (eV/atom). Experimental $B_0$ in GPa and $B_0'$ from ultrasonic data at ambient pressure [42]. PBE, HF, and PBE0 results are from self-consistent Kohn-Sham calculations; unmarked Power and Müller rows are from the present RDMFT calculations.

| Method | $a_0$ | $B_0$ | $B_0'$ | $E_0$ |
|---|---|---|---|---|
| Expt. | 10.26 | 97.9 | 4.24 | |
| PBE | 10.37 | 86.9 | 4.34 | −107.165 |
| HF | 10.36 | 105.2 | 3.91 | −103.542 |
| PBE0 | 10.31 | 96.9 | 4.19 | −107.237 |
| Power($\alpha = 0.70$)[a] | 10.55 | | | |
| Power | 10.31 | 94.5 | 4.54 | −104.395 |
| Müller[a] | 10.49 | | | |
| Müller | 10.20 | 81.2 | 4.84 | −107.840 |

[a] Ref. [14].

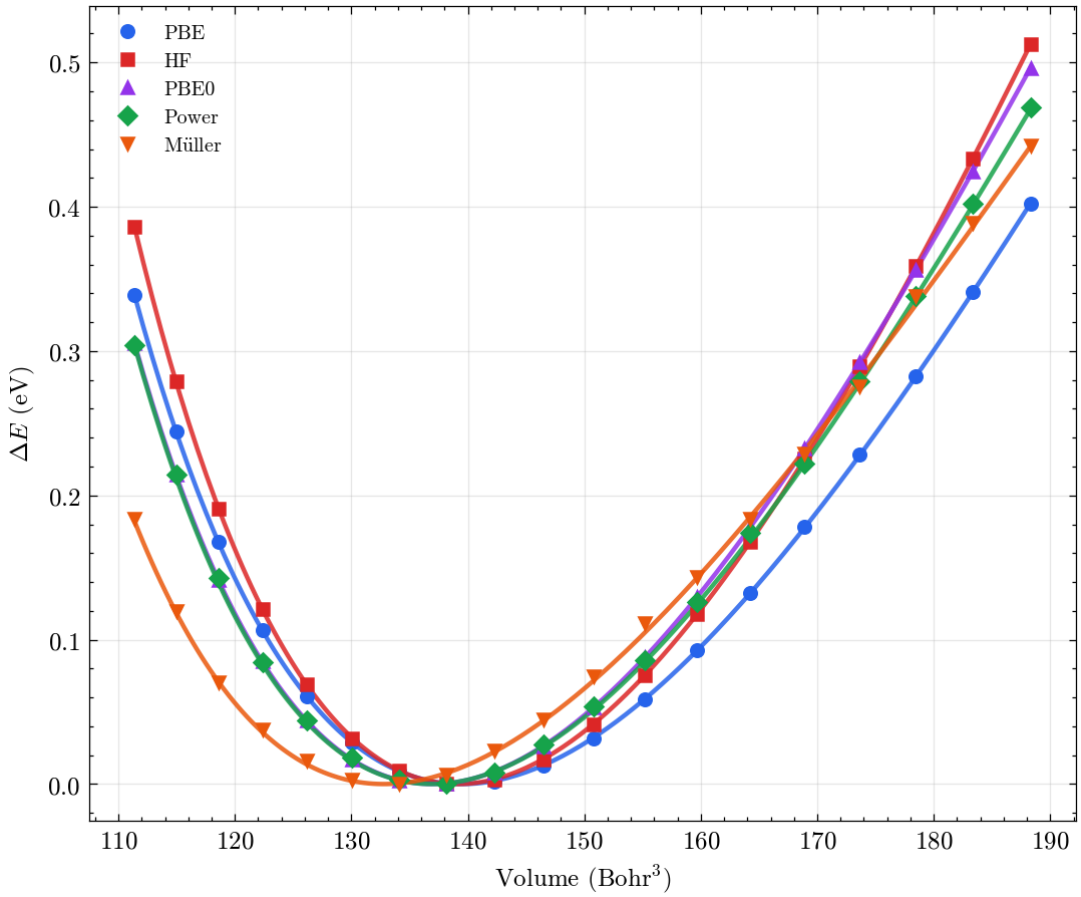


FIG. 6. Silicon EOS from RDMFT power and Müller functionals, compared with PBE, HF, and PBE0 references. Energy and volume are per atom. Energy is relative to the equilibrium energy per atom.

to deliberate perturbations of the initial occupations, whereas EBI can stall when occupations approach 0 or 1. Fractionally charged LiH and the silicon equation of state demonstrate applications beyond idempotent HF, including comparison with earlier RDMFT data and with standard DFT references. Our SPG occupation optimizer is more robust than the first-order EBI for both periodic and isolated systems. To further assess the original more-expensive second-order EBI in periodic systems and the box-aware gradient descent of ELK, a more systematic comparison study of these occupation optimizers is left for future work.

The natural next steps toward more efficient calculations include better preconditioners for the occupation and orbital blocks, fewer ACE rebuilds for large $k$-meshes, and support for a wider class of multi-channel XC kernels. A

stable optimizer also matters for functional development: when the solver converges reliably, one can compare XC approximations without wondering whether an apparent failure is only an incomplete minimization. The present implementation should make such comparisons easier for solids, and we hope it will help in refining existing RDMFT functionals and in constructing new ones that better describe strongly correlated systems that cannot be described by standard DFT.

Beyond total energies, the present framework naturally provides access to several experimentally relevant observables. The electron momentum density follows directly from the 1-RDM and can be compared with Compton scattering and $(e, 2e)$ experiments. Extending the method to describe spectral properties [43], such as the density of states and spectral functions, remains an important challenge, requiring either a dynamical formulation or a suitable reconstruction from the optimized natural orbitals and occupation numbers. The current occupation-orbital optimization framework is also readily applicable to spin-polarized and magnetic systems, including open-shell molecules and magnetic solids. Finally, incorporating atomic forces and linear-response theory would enable molecular dynamics as well as the calculation of phonons, dielectric properties, and other response functions within periodic RDMFT.

## ACKNOWLEDGMENTS

K. Luo is grateful for the auspices of the university internal grant No. AS392201. X. G. Ren acknowledges the funding support from Research and Development Program of China (Grant Nos. 2023YFA1507004 and 2022YFA1403800), and from the National Natural Science Foundation of China (Grant Nos. 12374067, 12134012, and 12188101).

## Appendix A: Projector $P_w$ in SPG

SPG [30] uses the Euclidean inner product throughout the inner loop: the chord slope is $\phi'(0) = \mathsf{g}^\top \mathsf{d}_k$ Eq. (36) and the stopping map is $\|\mathsf{g}_1\|_\infty$ Eq. (34). The repair map must therefore be the $\ell_2$ closest-point projection onto $\Omega$ Eq. (31) [30, 31],

$$P_w(\mathsf{x}) = \arg\min_{\mathsf{n}\in\Omega} \ \tfrac{1}{2}\sum_{i\mathbf{k}} (n_{i\mathbf{k}} - x_{i\mathbf{k}})^2. \tag{A1}$$

*Clip-shift form.* Expanding the constraints in Eq. (31), introduce a multiplier $\lambda$ for $\sum_{i\mathbf{k}} w_{\mathbf{k}} n_{i\mathbf{k}} = N_e$ and multipliers $\mu_{i\mathbf{k}}, \nu_{i\mathbf{k}} \geq 0$ for $n_{i\mathbf{k}} \geq 0$ and $1 - n_{i\mathbf{k}} \geq 0$:

$$\mathcal{L} = \tfrac{1}{2}\sum_{i\mathbf{k}} (n_{i\mathbf{k}} - x_{i\mathbf{k}})^2 + \lambda\left(\sum_{i\mathbf{k}} w_{\mathbf{k}} n_{i\mathbf{k}} - N_e\right) - \sum_{i\mathbf{k}} \mu_{i\mathbf{k}}\, n_{i\mathbf{k}} - \sum_{i\mathbf{k}} \nu_{i\mathbf{k}}\,(1 - n_{i\mathbf{k}}). \tag{A2}$$

Stationarity $\partial\mathcal{L}/\partial n_{i\mathbf{k}} = 0$ gives

$$n_{i\mathbf{k}} - x_{i\mathbf{k}} + \lambda w_{\mathbf{k}} - \mu_{i\mathbf{k}} + \nu_{i\mathbf{k}} = 0. \tag{A3}$$

With $s_{i\mathbf{k}} \equiv x_{i\mathbf{k}} - \lambda w_{\mathbf{k}}$ and complementarity ($\mu_{i\mathbf{k}} n_{i\mathbf{k}} = \nu_{i\mathbf{k}}(1 - n_{i\mathbf{k}}) = 0$), each component satisfies

$$n_{i\mathbf{k}} = \begin{cases} s_{i\mathbf{k}}, & 0 \leq s_{i\mathbf{k}} \leq 1, \\ 0, & s_{i\mathbf{k}} < 0, \\ 1, & s_{i\mathbf{k}} > 1, \end{cases} \tag{A4}$$

at the physical endpoints 0 and 1 [Eq. (8)]. This is Eq. (32), with $\lambda$ fixed by Eq. (33). The factor $w_{\mathbf{k}}$ in $s_{i\mathbf{k}}$ is the Lagrange multiplier of the weighted electron-count constraint, not a separate weighting of the projection metric.

*Initial descent.* Because $P_w$ is Euclidean projection onto convex $\Omega$, BMR Lemma 2.1 [30] gives $\phi'(0) < 0$ whenever $\mathsf{d}_k \neq \mathsf{0}$, as required by Eq. (36).

## Appendix B: Power-functional regularisation

For the separable power kernel $g(n) = n^\alpha$ with $\alpha \in (\frac{1}{2}, 1)$, the derivative $g'(n) = \alpha n^{\alpha-1}$ diverges as $n \to 0^+$. To obtain a finite coupling and occupation gradient for line searches, $g(n)$ is replaced below a floor $n_{\min} = \varepsilon$ by its

tangent at $n = \varepsilon$:

$$g(n) = \begin{cases} n^\alpha, & n \geq \varepsilon, \\ \varepsilon^\alpha + \alpha\, \varepsilon^{\alpha-1}(n - \varepsilon), & n < \varepsilon, \end{cases} \tag{B1}$$

with derivative

$$g'(n) = \alpha\, \max(n, \varepsilon)^{\alpha-1}. \tag{B2}$$

The piecewise definitions coincide at $n = \varepsilon$: $g(\varepsilon) = \varepsilon^\alpha$ and $g'(\varepsilon) = \alpha\, \varepsilon^{\alpha-1}$ from either branch, so $g$ and $g'$ are continuous at the join. Equations (B1) and (B2) enter the evaluation of $E_{\mathrm{xc}}$ and its occupation derivatives on equal footing. The default floor is $\varepsilon = 10^{-8}$.


[1] P. Hohenberg and W. Kohn, Inhomogeneous electron gas, Phys. Rev. **136**, B864 (1964).
[2] W. Kohn and L. J. Sham, Self-consistent equations including exchange and correlation effects, Phys. Rev. **140**, A1133 (1965).
[3] T. L. Gilbert, Hohenberg-kohn theorem for nonlocal external potentials, Phys. Rev. B **12**, 2111 (1975).
[4] A. M. K. Muller, Explicit approximate relation between reduced two- and one-particle density matrices, Phys. Lett. A **105**, 446 (1984).
[5] K. Pernal and K. J. H. Giesbertz, Reduced density matrix functional theory (rdmft) and linear response time-dependent rdmft (td-rdmft), in *Density-Functional Methods for Excited States*, edited by N. Ferre, M. Filatov, and M. Huix-Rotllant (Springer International Publishing, Cham, 2016) pp. 125–183.
[6] M. A. BUIJSE and E. J. BAERENDS, An approximate exchange-correlation hole density as a functional of the natural orbitals, Molecular Physics **100**, 401 (2002), https://doi.org/10.1080/00268970110070243.
[7] S. Goedecker and C. J. Umrigar, Natural orbital functional for the many-electron problem, Phys. Rev. Lett. **81**, 866 (1998).
[8] O. Gritsenko, K. Pernal, and E. J. Baerends, An improved density matrix functional by physically motivated repulsive corrections, The Journal of Chemical Physics **122**, 204102 (2005).
[9] G. Csányi and T. A. Arias, Tensor product expansions for correlation in quantum many-body systems, Phys. Rev. B **61**, 7348 (2000).
[10] G. Csányi, S. Goedecker, and T. A. Arias, Improved tensor-product expansions for the two-particle density matrix, Phys. Rev. A **65**, 032510 (2002).
[11] K. Pernal, The equivalence of the piris natural orbital functional 5 (PNOF5) and the antisymmetrized product of strongly orthogonal geminal theory, Computational and Theoretical Chemistry **1003**, 127 (2013), reduced Density Matrices: A Simpler Approach to Many-Electron Problems?
[12] K. Pernal, Long-range density-matrix-functional theory: Application to a modified homogeneous electron gas, Phys. Rev. A **81**, 052511 (2010).
[13] W. Ai, N. Q. Su, and W.-H. Fang, Short-range screened density matrix functional for proper descriptions of thermochemistry, thermochemical kinetics, nonbonded interactions, and singlet diradicals, The Journal of Chemical Physics **159**, 174110 (2023).
[14] S. Sharma, J. K. Dewhurst, N. N. Lathiotakis, and E. K. U. Gross, Reduced density matrix functional for many-electron systems, Phys. Rev. B **78**, 201103 (2008).
[15] T. Baldsiefen, A. Cangi, F. G. Eich, and E. K. U. Gross, Exchange-correlation approximations for reduced-density-matrix-functional theory at finite temperature: Capturing magnetic phase transitions in the homogeneous electron gas, Phys. Rev. A **96**, 062508 (2017).
[16] M. Vladaj, Q. Marécat, B. Senjean, and M. Saubanère, Variational minimization scheme for the one-particle reduced density matrix functional theory in the ensemble n-representability domain, The Journal of Chemical Physics **161**, 074105 (2024).
[17] M. Piris and I. Mitxelena, Donof: An open-source implementation of natural-orbital-functional-based methods for quantum chemistry, Comput. Phys. Commun. **259**, 107651 (2021).
[18] J. F. H. Lew-Yee, I. Mitxelena, J. M. del Campo, and M. Piris, Donof 2.0: A modern open-source electronic structure program for natural orbital functionals, The Journal of Chemical Physics **164**, 072501 (2026).
[19] The Elk Code, `http://elk.sourceforge.net/`.
[20] P. Giannozzi, S. Baroni, N. Bonini, M. Calandra, R. Car, C. Cavazzoni, D. Ceresoli, G. L. Chiarotti, M. Cococcioni, I. Dabo, A. Dal Corso, S. de Gironcoli, S. Fabris, G. Fratesi, R. Gebauer, U. Gerstmann, C. Gougoussis, A. Kokalj, M. Lazzeri, L. Martin-Samos, N. Marzari, F. Mauri, R. Mazzarello, S. Paolini, A. Pasquarello, L. Paulatto, C. Sbraccia, S. Scandolo, G. Sclauzero, A. P. Seitsonen, A. Smogunov, P. Umari, and R. M. Wentzcovitch, Quantum espresso: a modular and open-source software project for quantum simulations of materials, Journal of Physics: Condensed Matter **21**, 395502 (2009).
[21] K. Luo, T. Wang, and X. Ren, Direct minimization on the complex stiefel manifold in kohn-sham density functional theory for finite and extended systems, Computer Physics Communications **312**, 109596 (2025).

[22] L. Lin, Adaptively compressed exchange operator, Journal of Chemical Theory and Computation **12**, 2242 (2016), pMID: 27045571, https://doi.org/10.1021/acs.jctc.6b00092.

[23] P.-O. Löwdin, Quantum theory of many-particle systems. i. physical interpretations by means of density matrices, natural spin-orbitals, and convergence problems in the method of configurational interaction, Phys. Rev. **97**, 1474 (1955).

[24] A. J. Coleman, Density matrices of n-fermion systems, Canadian Mathematical Bulletin **4**, 209–212 (1961).

[25] A. J. Coleman, Structure of fermion density matrices, Rev. Mod. Phys. **35**, 668 (1963).

[26] F. Gygi and A. Baldereschi, Self-consistent hartree-fock and screened-exchange calculations in solids: Application to silicon, Phys. Rev. B **34**, 4405(R) (1986).

[27] H. W. Kuhn and A. W. Tucker, Nonlinear programming, in *Traces and Emergence of Nonlinear Programming*, edited by G. Giorgi and T. H. Kjeldsen (Springer Basel, Basel, 2014) pp. 247–258.

[28] Y. F. Yao, W. H. Fang, and N. Q. Su, Handling ensemble n-representability constraint in explicit-by-implicit manner, J. Phys. Chem. Lett. **12**, 6788 (2021).

[29] Y.-F. Yao, Z. Zhang, W.-H. Fang, and N. Q. Su, Explicit-by-implicit treatment of natural orbital occupations using first- and second-order optimization algorithms: A comparative study, The Journal of Physical Chemistry A **126**, 5654 (2022), pMID: 35950981, https://doi.org/10.1021/acs.jpca.2c02345.

[30] E. G. Birgin, J. M. Martínez, and M. Raydan, Nonmonotone spectral projected gradient methods on convex sets, SIAM Journal on Optimization **10**, 1196 (2000), https://doi.org/10.1137/S1052623497330963.

[31] P. H. Calamai and J. J. Moré, Projected gradient methods for linearly constrained problems, Mathematical Programming **39**, 93 (1987).

[32] J. Barzilai and J. M. Borwein, Two-point step size gradient methods, IMA Journal of Numerical Analysis **8**, 141 (1988).

[33] L. Armijo, Minimization of functions having Lipschitz continuous first partial derivatives, Pacific Journal of Mathematics **16**, 1 (1966).

[34] L. Grippo, F. Lampariello, and S. Lucidi, A nonmonotone line search technique for Newton's method, SIAM Journal on Numerical Analysis **23**, 707 (1986).

[35] M. Schlipf and F. Gygi, Optimization algorithm for the generation of oncv pseudopotentials, Computer Physics Communications **196**, 36 (2015).

[36] G. J. Martyna and M. E. Tuckerman, A reciprocal space based method for treating long range interactions in ab initio and force-field-based calculations in clusters, The Journal of Chemical Physics **110**, 2810 (1999).

[37] N. G. Cartier and K. J. H. Giesbertz, Impact of parametrizations of the one-body reduced density matrix on the energy landscape, The Journal of Physical Chemistry Letters **16**, 3822 (2025), https://pubs.acs.org/jpclcd/article-pdf/16/15/3822/42039217/jz5c00308.pdf.

[38] P. Mori-Sánchez, A. J. Cohen, and W. Yang, Localization and delocalization errors in density functional theory and implications for band-gap prediction, Phys. Rev. Lett. **100**, 146401 (2008).

[39] C. Li and W. Yang, On the piecewise convex or concave nature of ground state energy as a function of fractional number of electrons for approximate density functionals, The Journal of Chemical Physics **146**, 074107 (2017).

[40] J. P. Perdew, K. Burke, and M. Ernzerhof, Generalized gradient approximation made simple, Phys. Rev. Lett. **77**, 3865 (1996).

[41] J. Wang and E. J. Baerends, Self-consistent-field method for correlated many-electron systems with an entropic cumulant energy, Phys. Rev. Lett. **128**, 013001 (2022).

[42] H. J. McSkimin and P. Andreatch, Elastic moduli of silicon vs hydrostatic pressure at 25.0°C and $-195.8°c$, J. Appl. Phys. **35**, 2161 (1964).

[43] S. Sharma, J. K. Dewhurst, S. Shallcross, and E. K. U. Gross, Spectral density and metal-insulator phase transition in mott insulators within reduced density matrix functional theory, Phys. Rev. Lett. **110**, 116403 (2013).